Lithospheric Dynamics and Electrical Anisotropy: Magnetotelluric Analysis in Southern Tibetan Plateau

Zhehan Liu[1], Sheng Jin[1,2*], Hao Dong[1,2*], Wenbo Wei[1,2], Gaofeng Ye[1,2] and Letian Zhang[1,2]
[1] School of Geophysics and Information Technology, China University of Geosciences, Beijing, China
[2] State Key Laboratory of Geological Processes and Mineral Resources, China University of Geosciences, Beijing, China

SUMMARY

The mechanisms driving stress-induced surface deformation in the Tibetan Plateau have been a topic of debate. This study utilizes magnetotelluric data to develop two-dimensional anisotropic electrical resistivity models of the crust and upper mantle along a profile in the southern Tibetan Plateau. Our models reveal extensive crustal conductive structures with two groups of distinct anisotropic electrical properties, i.e.: 1) near north-south oriented anisotropy in the middle crust, and 2) east-west oriented anisotropy in the lower crust. These observations align with the dominate N-S stress distribution of the Tibetan Plateau. The distinct anisotropic alignment may reflect the variations in deformation styles and rheology: brittle in the upper crust, semi-brittle in the middle crust, and viscous in the lower crust. The N-S directed anisotropy correlates with the N-S aligned fractures or microcracks filled with fluids in the near-brittle upper and middle crust, while the E-W aligned viscous melt pockets may explain the observed E-W anisotropic characteristics in the lower crust.

Keywords: Tibetan Plateau; magnetotellurics; electrical anisotropy; brittle deformation; viscous deformation

INTRODUCTION

As an important indicator of the deformation feature in the Earth's crust and mantle, the mechanisms and geodynamic implications of the lithospheric anisotropy remain a contentious topic. Underground anisotropy typically arises from stress and rock formation, with origins tied to shape-preferred orientation (SPO), lattice-preferred orientation (LPO), and crystal-preferred orientation (CPO) of Earth's materials (Boness & MD Zoback, 2006). Factors leading to anisotropy at different depths include fractures, microcracks, shear-aligned crystals, partial melt, graphitized shear zones, etc. (Valcke et al., 2006). In Tibetan Plateau, the extensive evidence of radial and azimuthal seismic anisotropy suggests widespread anisotropy features in the crust and mantle, especially in the doubly thickened Tibetan crust (Agius & Lebedev, 2017). On the other hand, the magnetotelluric (MT) is a popular method in resolving the geoelectrical information within the lithosphere (Unsworth et al., 2005). Conductivity anisotropy also can provide unique insights into the complex internal structures of the Earth. However, the understanding of electrical anisotropy in the Plateau remains limited. To address this, we explore the electrical anisotropy characteristics and geodynamic mechanisms in the southern Tibetan Plateau with 2-D anisotropic resistivity modeling methods.

METHODS

This study utilized twenty-six MT sites, comprising twenty-two broadband (BBMT) and four long-period (LMT) sites, including twenty-five SinoProbe (Dong et al., 2013) sites and one from line-3000 (Wei et al., 2001) (Figure 1).

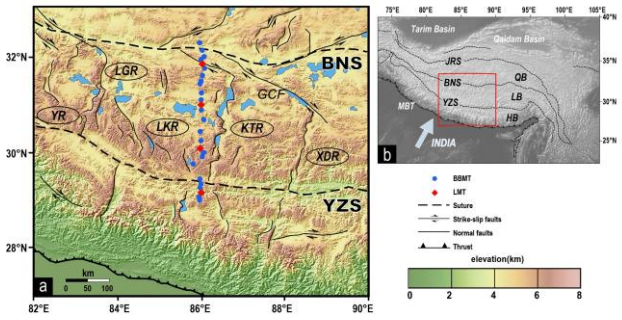

Figure 1. (a) topographic map of the study region showing major tectonic structures and magnetotelluric site locations. (b) Regional map highlighting the Tibetan Plateau and surrounding areas, with the study area outlined by a red rectangle.

We carried out the two-dimensional anisotropic inversions along the profile with the MARE2DEM software (Key, 2016), using Occam's method to generate smooth resistivity structure. Joint inversion of TE, TM, and tipper data was performed for the

period range of 0.01 to 10,000 s. The error floors were set at 5% for TM and TE mode phases, 10% for TM mode apparent resistivity, and 50% for TE mode apparent resistivity. Tipper components had a fixed error floor of 0.1. The air layer was modeled with a resistivity of 1.0×10^9 Ωm, and the subsurface resistivity was set to 100Ωm for the starting model. The model grid incorporated surface topography and consists of four layers with increasing size of model cells, from the surface to 100 km depth. The mesh size expands exponentially outside the core region.

In conducting anisotropic inversions, we targeted a normalized root-mean-square (RMS) misfit of 1 and set the horizontal-to-vertical smoothing ratio to 3 to emphasize horizontal features. Besides, we chose anisotropy penalty weight factor α =0.3. We reduced the initial RMS misfit from 8.67 to 1.4 over eight iterations. Using this model as the starting model, we then aimed for an RMS misfit of 1.4, achieving the smoothest model in three additional iterations.

We conducted extensive inversions to evaluate how changes in model parameters affect resistivity characteristics. Additionally, we performed synthetic inversion tests to verify the robustness of our model features. Ultimately, we incorporated two roughness penalty boundaries in the anisotropic resistivity model. These boundaries enable sharp transitions in the inverted resistivity, helping to prevent overfitting and enhancing the stability of the inversion process.

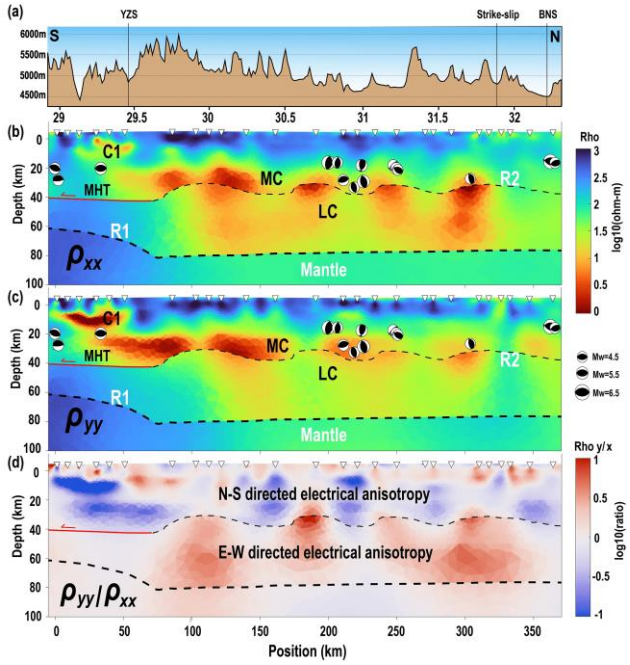

Figure 2. Preferred anisotropic resistivity model: (a) Profile topography. Resistivity structures for (b) the ρ_{xx} model, (c) the ρ_{yy} model, and (d) the ρ_{yy}/ρ_{xx} model. The red solid line and upper thin black dotted lines indicate the mid-to-lower crust electrical discontinuity (MLC-ED), while the lower thick dotted line marks the Moho discontinuity from Xu et al. (2015). Earthquake focal mechanisms were obtained from the Global Centroid Moment Tensor (GCMT) database

Figure 2 shows the preferred anisotropic resistivity model. The model reveals a relatively resistive upper crust and a prominent conductive mid-to-lower crust. Interestingly, the ρ_{yy}/ρ_{xx} model reveals a double-layer anisotropy structure in the mid-to-lower crust, with strongly anisotropic regions corresponding closely to conductive structures. One anisotropic layer is identified at a depth of approximately 20-35 km, and another layer extends from 35 km to the upper mantle, potentially marking the boundary between the middle and lower crust. The red solid and black dotted lines in Figure 2 indicate the upper boundary, representing the electrical anisotropy discontinuity between the middle and lower crust. We refer to this as the mid-to-lower crust electrical discontinuity (MLC-ED). The lower boundary corresponds to the Moho discontinuity, as proposed by Xu et al. (2015).

RESULTS

The upper crust (<20 km) exhibits high resistivity (100-1000 Ωm) features and aligns with extensive Mesozoic-Cenozoic granite and the Gangdese batholiths (Zhu et al., 2013). On the profile's southern side, a high-resistivity body lies below the Main Himalayan thrust (MHT) with a significantly low degree of electrical anisotropy, corresponding to the subducting Indian plate. The most distinctive feature of the mid-to-lower crust is the highly conductive layers, beginning at ~20 km depth and extending to 55-60 km (According to our boundary tests). Notably, these layers exhibit different preferred orientations of electrical anisotropy above and below the MLC-ED. Specifically, the middle crust conductors have lower resistivity in the y direction, showing nearly N-S directed anisotropy features. Conversely, the lower crust conductors have lower resistivity in the x direction, displaying nearly E-W directed anisotropy features. We utilize effective bulk conductivity to examine conductivity anomalies and electrical anisotropy (Rippe & Unsworth, 2010). This analysis reveals that in the mid-to-lower crust, the effective bulk conductivity can reach 0.1-0.5 S/m, and the maximum magnitude of electrical anisotropy can reach 3-5 times.

Explaining the origins of high conductivity and crustal electrical anisotropy is crucial. For the middle crust, we attribute the high conductivity to a combination of the dehydrogenation of amphibole and aqueous fluids. In the lower crust, we primarily

attribute the high conductivity to the dehydration melting of amphibole.

With the help of the Petrology deformation experiments, we establish the relationships between conductivity, melt fraction (Guo et al., 2018), and viscosity distribution (Liu & Hasterok, 2016) of the viscous lower crust. Our analysis accommodates melt fractions ranging from 6% to 27%, with viscosity values generally below 10^{19} Pa·s. Quantifying viscosity values for the un-melted middle crust is difficult; however, we consider that its deformation can be characterized as a semi-brittle mode. This semi-brittle behavior represents a transitional state between the brittle failure observed in the upper crust and the viscous flow in the lower crust (Reber et al., 2020); in this phase, both intracrystalline viscosity and brittle failure are integral mechanisms.

DISCUSSION

The resistivity model reveals two distinct anisotropic layers separated by the MLC-ED. The differing preferred orientations of electric currents in these layers likely reflect the complex material compositions and tectonic processes of the Tibetan Plateau. Therefore, we propose a "bilayer electrical anisotropy model" (Figure 3) to accommodate the different deformation mechanisms arising from variations in material composition and structure characteristics.

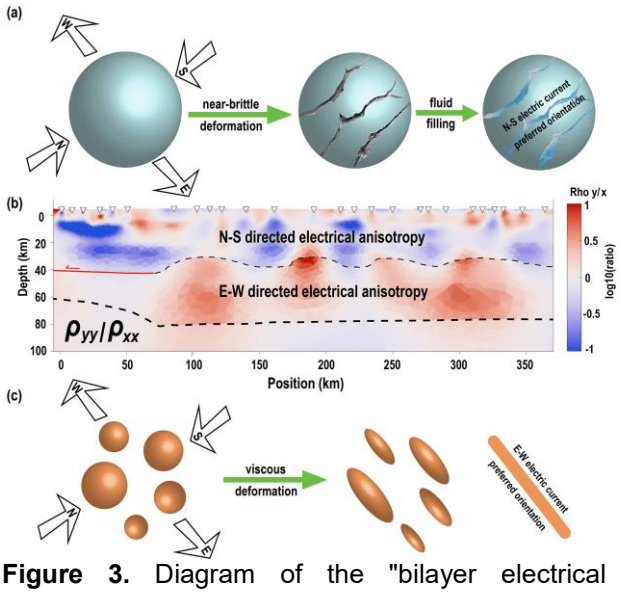

Figure 3. Diagram of the "bilayer electrical anisotropy model": (a) Schematic shows the structure of near-brittle deformation, where electric current primarily flows along nearly north-south fractures. (b) The electrical anisotropic model is the same as Figure 2d. (c) Schematic illustrates viscous deformation, with electric current flowing along the long axis of ellipsoidal melt.

Crustal anisotropy is primarily driven by the converging compressional forces of the Indian-Eurasian plates; intense compressive stress permeates the entire crustal environment. Under the nearly N-S axial compression, the viscous melt pockets in the lower crust elongate along the E-W direction due to the squeezing stress, and electric current flows more readily in the E-W direction, exhibiting an E-W directed electrical anisotropy feature (Figure 3c). The middle crust is mainly un-melted and lacks viscous rheological capability. Thus, the compressive stress in the N-S direction has compacted the materials. When subjected to extensional stress in the E-W direction, semi-brittle fracturing with micro-porosity occurs along the nearly N-S orientation (Figure 3a). With the assistance of the fluid, the nearly N-S directed electric current preferred orientations govern the middle crust anisotropic features. In the upper crust, the electrical anisotropy can be unevenly distributed considering fractures, lithological heterogeneities, and variations in dips of graben. The deformation mode of the upper crust is similar to that of the middle crust, demonstrating electrical anisotropy features primarily in the N-S direction (Figure 3a). Still, as the confining pressure decreases, microcracks can gradually develop into macroscopic fractures and normal faults in the graben systems.

CONCLUSIONS

In this study, we developed two-dimensional anisotropic resistivity models using magnetotelluric data from the southern Tibetan Plateau. Our models reveal a complex crustal deformation pattern, highlighting changes in electrical anisotropy features from deep to shallow depths, suggesting variations in crustal rheology characteristics. We propose a "bilayer electrical anisotropy model" to systematically explain crustal anisotropy origins, emphasizing compression stress from plate convergence as the primary factor. The Tibetan Plateau adapts to north-south shortening and east-west extension through pure shear deformation. The lower crust displays an east-west directed anisotropy, predominantly influenced by viscous deformation, while the upper-middle crust exhibits north-south directed anisotropy due to near-brittle deformation. We attribute lower crust conductivity anomalies to partial melts and middle crust conductivity anomalies to amphibole dehydrogenation and aqueous fluids.

ACKNOWLEDGEMENTS

The Second Tibetan Plateau Scientific Expedition and Research Program (2019QZKK0701) and the National Natural Science Foundation of China (42274098) provided funding for this study.

References

Agius, M. R., & Lebedev, S. (2017). Complex, multilayered azimuthal anisotropy beneath Tibet: evidence for co-existing channel flow and pure-shear crustal thickening. *Geophysical Journal International*, *210*(3), 1823–1844. https://doi.org/10.1093/gji/ggx266

Boness, N. L. & MD Zoback. (2006). Mapping stress and structurally controlled crustal shear velocity anisotropy in California. *Geology*, *34*(10), 825–828. https://doi.org/10.1130/G22309.1

Dong, S. W., Li, T. D., QT Lü, Gao, R., Yang, J. S., Chen, X. H., et al. (2013). Progress in deep lithospheric exploration of the continental China: A review of the SinoProbe. *Tectonophysics*, *606*, 1–13.

Guo, X., Zhang, L., Su, X., Mao, Z., Gao, X.-Y., Yang, X., & Ni, H. (2018). Melting Inside the Tibetan Crust? Constraint From Electrical Conductivity of Peraluminous Granitic Melt. *Geophysical Research Letters*, *45*(9), 3906–3913. https://doi.org/10.1029/2018GL077804

Key, K. (2016). MARE2DEM: a 2-D inversion code for controlled-source electromagnetic and magnetotelluric data. *Geophysical Journal International*, *207*(1), 571–588. https://doi.org/10.1093/gji/ggw290

Liu, L., & Hasterok, D. (2016). High-resolution lithosphere viscosity and dynamics revealed by magnetotelluric imaging. *Science*, *353*(6307), 1515–1519. https://doi.org/10.1126/science.aaf6542

Reber, J. E., Cooke, M. L., & Dooley, T. P. (2020). What model material to use? A Review on rock analogs for structural geology and tectonics. *Earth-Science Reviews*, *202*, 103107. https://doi.org/10.1016/j.earscirev.2020.103107

Rippe, D., & Unsworth, M. (2010). Quantifying crustal flow in Tibet with magnetotelluric data. *Physics of the Earth and Planetary Interiors*, *179*(3), 107–121. https://doi.org/10.1016/j.pepi.2010.01.009

Unsworth, M. J., Jones, A. G., Wei, W., Marquis, G., Gokarn, S. G., & Spratt, J. E. (2005). Crustal rheology of the Himalaya and Southern Tibet inferred from magnetotelluric data. *Nature*, *438*(7064), 78–81. https://doi.org/10.1038/nature04154

Valcke, S. L. A., Casey, M., Lloyd, G. E., Kendall, J.-M., & Fisher, Q. J. (2006). Lattice preferred orientation and seismic anisotropy in sedimentary rocks. *Geophysical Journal International*, *166*(2), 652–666. https://doi.org/10.1111/j.1365-246X.2006.02987.x

Wei, W., Unsworth, M., Jones, A., Booker, J., Tan, H., Nelson, D., et al. (2001). Detection of Widespread Fluids in the Tibetan Crust by Magnetotelluric Studies. *Science*, *292*(5517), 716–719. https://doi.org/10.1126/science.1010580

Xu, Q., Zhao, J., Yuan, X., Liu, H., & Pei, S. (2015). Mapping crustal structure beneath southern Tibet: Seismic evidence for continental crustal underthrusting. *Gondwana Research*, *27*(4), 1487–1493. https://doi.org/10.1016/j.gr.2014.01.006

Zhu, D., Zhao, Z., Niu, Y., Dilek, Y., Hou, Z.-Q., & Mo, X.-X. (2013). The origin and pre-Cenozoic evolution of the Tibetan Plateau. *Gondwana Research*, *23*(4), 1429–1454. https://doi.org/10.1016/j.gr.2012.02.002